Corrosion Science 207 (2022) 110550

Contents lists available at ScienceDirect

Corrosion Science

journal homepage: www.elsevier.com/locate/corsci

Influence of the surface state on the corrosion behavior of the 316 L stainless steel manufactured by laser powder bed fusion

J. Bedmar *, N. Abu-warda, S. García-Rodríguez, B. Torres, J. Rams

Dpto. de Matemática Aplicada, Ciencia e Ingeniería de Materiales y Tecnología Electrónica, ESCET, Universidad Rey Juan Carlos, Tulipán s/n, 28933 Móstoles, Madrid, Spain

ARTICLE INFO

Keywords:
316 L stainless steel
Additive manufacturing
Laser powder bed fusion
Surface roughness
Corrosion
Oxidation

ABSTRACT

The effect of surface roughness on the corrosion behavior of 316 L stainless steel manufactured by LPBF has been evaluated. The behavior of the steel in the as-built state was compared to that ground up to 2500 grade. Three different aggressive environments were used: 3.5 wt% NaCl water solution, 3 wt% H_2SO_4 solution, and high-temperature oxidation at 800 °C. The ground specimens showed higher corrosion resistance. The corrosion resistance was much smaller in the as-built samples for electrochemical tests, and the lowest mass gain after high-temperature oxidation was found in the ground specimens.

1. Introduction

Laser Powder Bed Fusion (LPBF) is a group of techniques belonging to additive manufacturing (AM). LPBF consists of the melting of a layer of powder after its deposition in a powder bed thanks to a laser source in an inert atmosphere, such as Argon, to avoid undesirable reactions in the hot metal [1]. This process has many advantages, such as the fabrication of near-net-shape parts without the need of using molds or the possibility of fabricating pieces with complex geometries [2]. On the other hand, several drawbacks can be found such as the presence of porosity [3], anisotropy [4], or roughness [5], which is higher than in parts fabricated by conventional methods like mechanizing or casting [6]. Roughness is very important since many important applications require roughness below 0.8 μm [7], something which is difficult to reach is as-built LPBF parts [8].

Particularly, surface roughness has been studied as a defect of the parts fabricated by LPBF. It is affected by the different variables that influence the manufacturing process such as the hatch distance or the stability of the laser used [9]. In this study, the LPBF printer was equipped with a fiber laser, which has a big influence on the properties of the fabricated specimens. Their emission is near-infrared, which gets a good absorptivity from the metals, and their optical components produce a high beam quality. However, its performance is limited by nonlinear effects in the gain medium and by polarization instabilities [10]. Despite this, all the good qualities and advantages mentioned before have made these lasers the most commonly used ones in LPBF printers.

The manufacturing parameters must be precisely optimized, otherwise, they can generate the balling phenomenon [11]. Balling is caused because the laser molten track shrinks to reduce the surface energy as a result of the surface tension, giving rise to the presence of particles that form the surface of parts with rounded shapes in the last layers. Two kinds of balling have been observed: ellipsoidal big balls that strongly degrade the properties of the pieces, which is caused by bad wettability; and small rounded balls, which have been found not to have equivalent negative effects [12]. Balling limits the final accuracy of the shape of the samples and reduces the wear performance [13] and the fatigue life, and promotes the surface cracking of the samples [14]. The last layer is not the only one affected by balling. It has been observed that the balling phenomenon can affect the distribution and the homogeneity of the powder when it is deposited during the fabrication in the powder bed, causing poor welding between layers, which can cause delaminations or poor resistance to fatigue, as well as other changes in the performance of the pieces. [15].

316 L stainless steel is one of the most used alloys to fabricate parts by LPBF systems thanks to its good weldability [16] and its ease to be processed [17]. This austenitic stainless steel is well known for its good mechanical properties, wear, and corrosion behavior [18], and its wide range of possible applications, like in the health sector [19], the transport field [20], or the energy industry [21]. In this sense, additive manufacturing can provide unique and personalized parts, which is important in the sectors where only a small series of fabrication are

* Corresponding author.
E-mail address: javier.bedmar@urjc.es (J. Bedmar).

https://doi.org/10.1016/j.corsci.2022.110550
Received 22 April 2022; Received in revised form 26 July 2022; Accepted 28 July 2022
Available online 30 July 2022

needed, as mentioned before. Although the 316 L stainless steel fabricated by LPBF can exceed different properties of this alloy manufactured by conventional methods [22], [23]; different problems have been reported in previous studies, like the cited porosity, anisotropy, or surface roughness.

To reduce these disadvantages, different postprocessing techniques have been investigated, like the heat treatments [24], the hot isostatic pressing [25], or the laser shock peening [26]. In the case of surface roughness, several techniques have been investigated. In this sense, Tyagi et al. studied the influence of electropolishing and chempolishing on the surface of 316 L ss parts made by LPBF [27]. They found that both, electropolishing and chempolishing, can bring down the internal and external surface roughness, while other methods like the grounding can only be used for the external surface. However, the most studied technique to reduce it is machining. It has been claimed that machining improved the accuracy, the mechanical properties, and the wear behavior of the parts [28]. Also, the material removed by machining is much less in AM than in parts manufactured by conventional techniques. However, machining modifies the surface of the samples, so it is important to analyze how it affects other relevant properties of the material such as the corrosion behavior. Moreover, the analysis of surface finishing effects on the corrosion behavior is particularly important in AM samples as the complex geometries often obtained by AM (e.g. lattice, tubes, etc.) makes it impossible to apply any surface modification technique. Therefore, it is essential to understand how the surface finishing affects the corrosion resistance of materials manufactured by SLM.

In this work, the influence of the surface finishing on the corrosion resistance of the 316 L stainless steel manufactured by an LPBF system has been studied. As-built and ground parts have been exposed to three different corrosive environments: 3.5% NaCl water solution, 0.1 M H_2SO_4 water solution, and oxidation at high temperature in dry air (800 °C). These different conditions allow a deep and complete study of the role that the surface roughness of LPBF plays on the corrosion behavior and how the machining used to improve the mechanical properties of the 316 L stainless steel influences its corrosion.

2. Experimental procedure

2.1. Materials

316 L stainless steel plates were manufactured with an LPBF system equipped with a fiber laser (EOS M280 400 W). The laser beam used for the fabrication had a wavelength of 1070 nm with a Gaussian shape, a power of 195 W, and the laser spot had a diameter of 0.07 mm. The scanning speed of the process was 1083 mm/s, the laser height was 20 μm, the hatching distance was 90 μm and the infill angle varied of 67° between layers. The particle size of the powder was in the range of 20–50 μm.

The chemical composition of 316 L stainless steel (in wt%), determined by X-ray fluorescence analysis with a Philips Panalitycal MagiX, was 17.0 Cr, 13.1 Ni, 2.7 Mo, 1.3 Mn, 1.2 Si, ≤ 0.1 O, ≤ 0.03 C and balance Fe. The samples, with a size of 15 × 15 × 1.5 (in mm), were manufactured following the build direction shown in Fig. 1. Two different surface finishings have been tested: (i) the surface with the roughness obtained in the as-received state, hereafter 316 L-As Built (316 L-AB), and (ii) a ground surface obtained by grounding the samples with SiC emery paper up to 2500 grade, hereafter 316 L-Ground (316 L-G). In all the ground samples, 24 h were waited to carry out the corrosion tests, with the intention that the passive layer was formed.

Archimedes' density method was used to measure density of the as-built parts. Every part was weighted in the air and immersed in water and the Archimedes density, ρ, was obtained by the Eq. 1:

$$\rho = \frac{W(a)}{0.99967} \frac{[\rho(fl) - \rho(a)]}{[W(a) - W(fl)]} + \rho(a) \quad (1)$$

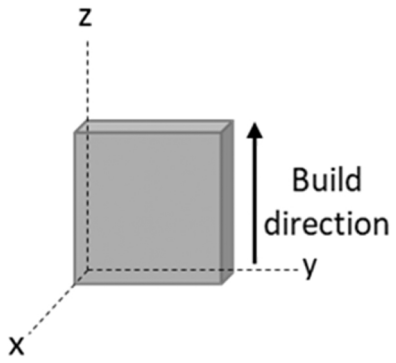

Fig. 1. Schematic representation of the build direction of the manufacturing process.

Where $W(a)$ is the weight of the part measured in the air; $\rho(fl)$, the density of the water in which the part is immersed counting with its temperature; $\rho(a)$, the air density in room conditions; and $W(fl)$, the weight of the part immersed in water. The density of the as-built parts was 7.94 ± 0.02 g/cm^3, which implies a relative density of 99.25% ± 0.25%, i.e. a porosity of 0.75%.

2.2. Corrosion tests

2.2.1. Immersion tests

Immersion tests were performed in 316 L-AB and 316 L-G samples. The different samples were fully immersed at room temperature in a vertical position in a 3.5 wt% NaCl water solution and in 3 wt% H_2SO_4. The immersion times in the 3 wt% H_2SO_4 solution were 1, 24, 48, 120, 216, and 360 h. For the 3.5 wt% NaCl solution the immersion times extended for up to 1008 h. Samples were weighed before and after each immersion time to obtain the mass gain. Before weighing them, samples were cleaned with warm water and dried with hot air. At least two samples were immersed in the different media to ensure the reproducibility of the results.

2.2.2. Electrochemical tests

Electrochemical tests were carried out in the 3.5 wt% NaCl and 3 wt % H_2SO_4 solutions at room temperature using an Autolab PGStat302N potentiostat provided with Nova 2.1 software. For the different measurements, a three-electrode cell configuration was used, where the working electrode was the additive manufactured stainless steel sample (316 L-AB or 316 L-G), the reference electrode was a silver/silver chloride (Ag/AgCl), and the counter electrode was a graphite rod. The tested sample was pressed against and opened in the electrochemical cell with a rubber O-ring, exposing an area of 0.76 cm^2 to the electrolyte. The studied surface of the samples were the ones parallel to the build direction, which is the YZ plane in Fig. 1.

The polarization resistance of the samples (R_p) was obtained by varying the potential from ± 10 mV around the corrosion potential (E_{corr}), using a 1 mV/s scanning rate. The tests were carried out for the different samples at different immersion times in the electrolyte solution: 1, 24, 48, 120, 216, and 360 h for 3 wt% H_2SO_4 solution and up to 1008 h for 3.5 wt% NaCl water solution, to study the evolution of R_p and E_{corr} with the immersion time.

Cyclic potentiodynamic tests were carried out to determine the susceptibility to localized corrosion. A polarization scan was carried out in the anodic direction, starting at − 1.4 V, at a rate of 0.1 V/s with a maximum and minimum potential of 1 V and −1.4 V, respectively, around the E_{corr}. The sweep direction was reversed at a limit threshold of 5 mA/cm^2. These tests were performed after 1 h of immersion by triplicate in different samples.

2.2.3. High-temperature oxidation

High-temperature oxidation tests were carried out in a dry air atmosphere at 800 ºC for 360 h to simulate real working conditions, using a Nabertherm LT 5/12/P330 furnace. The samples were placed individually in alumina crucibles and were weighed after 5, 24, 48, 120, 216, and 360 h of thermal test to obtain their mass gain versus exposure time. At least two samples were tested for each experimental condition to guarantee the reproducibility of the results.

2.3. Samples characterization

An optical profilometer (Zeta Instruments) was used to analyze the surface state and its area with the Zeta3D software. ImageJ was used to calculate the real area of the samples with the profiles obtained from the profilometer.

Samples were analyzed on the YZ-surface (see Fig. 1) and the cross-section after the different tests by Scanning Electron Microscopy (SEM, Hitachi S-3400 N). For microscopic characterization of the cross-section, metallographic samples were cut using a SiC disc cutter, hot mounted in conductive resin, ground with SiC emery paper up to 4000 grade, and polished with diamond paste to 1 μm.

X-ray diffraction (XRD) technique has been used to characterize the phases present in 316 L stainless steel before and after high-temperature oxidation tests and to analyze the grown oxides in the YZ-surface of the as-built and ground samples. A Panalytical X'Pert PRO diffractometer has been employed using monochromatic Cu Kα (1.54056 Å) as the radiation source with 45 kV and 40 mA. Diffraction patterns have been recorded in an angular interval of 10 – 120°, with the step of $\Delta(2\theta) = 0.04°$ and time per step of 1 s. The patterns have been indexed in the PDF-4 database of ICDD.

Surface roughness measurements of each sample were obtained with a Zeta-20 optical 3D profilometer with a resolution of 1 μm at × 20 magnifications and the Zeta-3D HDR optical configuration.

3. Results and discussion

3.1. Starting materials characterization

Fig. 2 shows the 3D optical profile of the plain view of the 316 L-AB and 316 L-G samples, where the surface morphology characteristics can be observed. There is a clear difference between the sample in the as-built state (316 L-AB) and the sample after the surface grounding process (316 L-G). The surface of the 316 L-AB (Fig. 2(a)) shows spherical-like zones of different sizes on the surface that correspond to the balling phenomenon characteristic of LPBF. On the other hand, the 316 L-G shows a very flat surface with minor grooves in the surface (Fig. 2(b)). The paper used, i.e. 2500 grit, corresponds with a particle size of 7.8 μm, so any surface feature should be well below this value.

From different images, the average surface roughness of 316 L-AB and 316 L-G samples was measured, and many different roughness parameters were obtained (Table 1). The average roughness (R_a) for the 316 L-AB samples was 2.8 ± 0.6 μm, while for the 316 L-G was 0.07 ± 0.01 μm, respectively. The difference in the most basic roughness parameters was 40 times it was slightly lower for R_z, i.e., in the difference between the highest points and the lowest ones. The variation of the other parameters indicates that the surfaces had similar morphologies but with different dimensions. Particularly, the kurtosis values (R_{ku}) were in both cases close to 3, but for the 316 L-AB the value was slightly above it, meaning that there were many zones far from the average line, while for the 316-G it was below 3, meaning that most of the material was in the average line with smaller contributions up and below it [29].

In most cases, the skewness (R_{sk}) was negative, indicating that in both cases the main peaks were below the average line; therefore, the valleys predominated over the peaks. The high value of the R_{pv} indicates the addition between the highest peak and the lowest valley in each sample, which was very big for the 316 L-AB sample, 17 μm, while was very small for the 316 L-G, 0.47 μm. Finally, developed interfacial area ratio (S_{dr}) values were calculated, as this indicates the percentage of the additional area of a surface contributed by texture as compared to a flat area [30].

As a general consideration, the 316 L-AB did not have a very high roughness, although it would be too high for some applications and would induce fatigue failures, while the roughness of the 316 L-G, was under the values required for the most demanding applications [7].

The phases present in the 316 L-AB and 316-L-G samples were identified by XRD, as is shown in Fig. 3. Diffraction patterns of both samples showed the same peaks, which correspond to the γ-Fe phase. However, a broadening of the peaks was observed in the as-built samples. Table 2 summarized the full width at half-maximum (FWHM) of the five main peaks γ-Fe observed in the XRD diagram. On average, the FWHM of the peaks was 80% greater in the as-built samples than in the ground ones. The peak with the smallest change of the five peaks

Table 1
Values of the surface roughness parameters of the studied specimens.

Parameter (μm)	316 L-AB	316 L-G
R_a	2.8 ± 0.6	0.07 ± 0.04
R_z	9.4 ± 1.5	0.36 ± 0.04
R_{pv}	17 ± 3	0.47 ± 0.12
R_{sk}	-0.4 ± 0.8	-0.24 ± 0.18
R_{ku}	3.2 ± 0.7	2.7 ± 0.6
S_{dr}	7.2 ± 0.5	0.15 ± 0.02

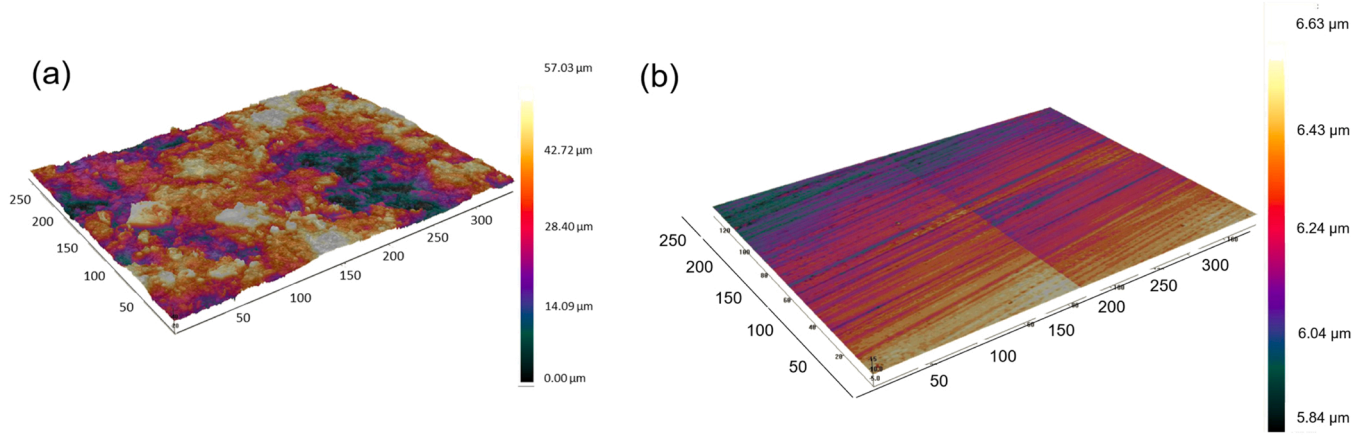

Fig. 2. 3D Optical profiler micrographs of (a) 316 L-AB and (b) 316 L-G samples.

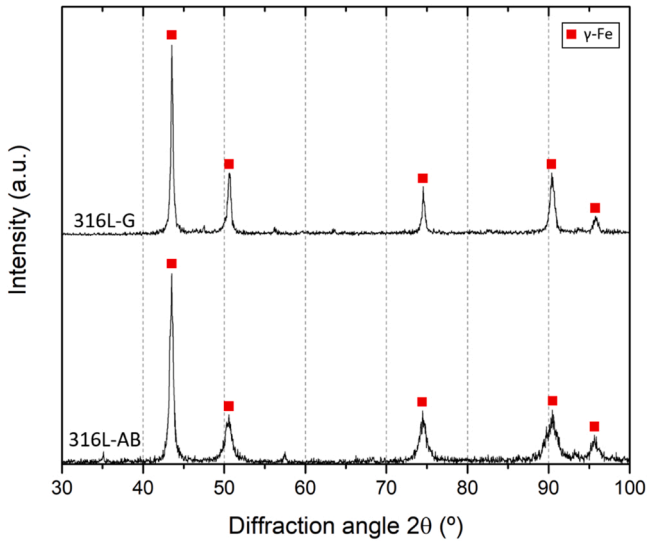

Fig. 3. X-ray diffraction analysis of the starting 316 L-AB and 316 L-G materials.

Table 2
Comparison of 2θ angle, FWHM, crystal size, and lattice strain for (111), (200), (220), (311), and (222) γ-Fe peaks for the two surface finishings.

Sample	Peak	γ-Fe 2θ (°)	γ-Fe peak FWHM (°)	Crystal size (Å)	Lattice strain (%)
316-AB	(111)	43.460	0.480	207	0.520
	(200)	50.470	0.787	124	0.725
	(220)	74.500	0.709	160	0.404
	(311)	90.360	0.945	137	0.406
	(222)	95.500	0.945	143	0.372
316-G	(111)	43.519	0.297	372	0.316
	(200)	50.555	0.440	241	0.400
	(220)	74.510	0.337	398	0.187
	(311)	90.347	0.554	260	0.235
	(222)	95.700	0.549	276	0.212

measured was the $(111)_{\gamma\text{-Fe}}$; the FWHM for the 316 L-AB and 316 L-G samples was 0.480° and 0.297°, respectively, which is a 62% higher value.

Peak broadening can be an indicator of grain size decrease and the presence of defects in the crystalline structure caused by a large local strain. An X-ray line broadening analysis was made to characterize surface microstructure in terms of crystal size and lattice strain. The crystal size of both samples was calculated using the Scherrer equation, and instrumental broadening of LaB_6 was used for this purpose. The average crystal size of 316 L-AB and 316 L-G samples, calculated with the results of each peak in Table 2, are ~154 and ~309 Å, respectively. This indicates that a decrease of crystal size by 50% takes place in the outer layers of the as-built samples. Also, this value is inversely proportional to lattice strain, indicating that the strain in the as-built samples was 82% greater than in the ground ones. Therefore, grounding nearly reduces by 50% the strain at the surface of the LPBF samples.

In addition, a slight shift in the position of the peaks was also noted, with most of the peaks of the as-built sample having smaller diffraction angles. This indicates that the distance between the atomic planes was smaller in the as-built sample, which indicates the presence of strain at the surface, as was also indicated by the width of the peaks.

The microstructure of both samples is shown in Fig. 4. The general microstructure, Fig. 4(a), is the typical one seen in the 316 L made by the LPBF process, composed of austenitic columnar grains which grow in the heat dissipation direction, as observed in other studies [31]. These columnar grains are slightly finer in the surface zones than in the inside of the parts, Fig. 4(b). These results coincide with others shown by other authors [32] and are caused by a faster solidification in the borders than in the inside of the specimens [28].

3.2. Immersion tests

Results of the mass change are shown in Fig. 5. It can be seen that there are not so many differences between the specimens as-built and the ground specimens and these differences are so small that they can be associated with the experimental deviation, so the original state of the

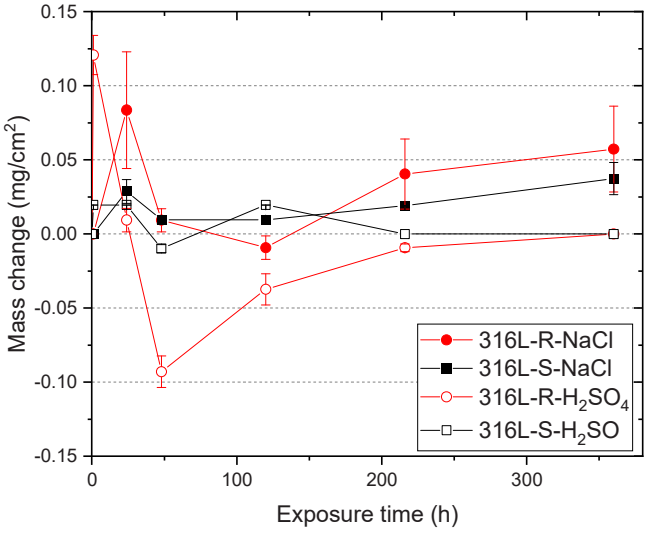

Fig. 5. Mass change after immersion tests in NaCl and H_2SO_4 solutions from 1 h to 360 h.

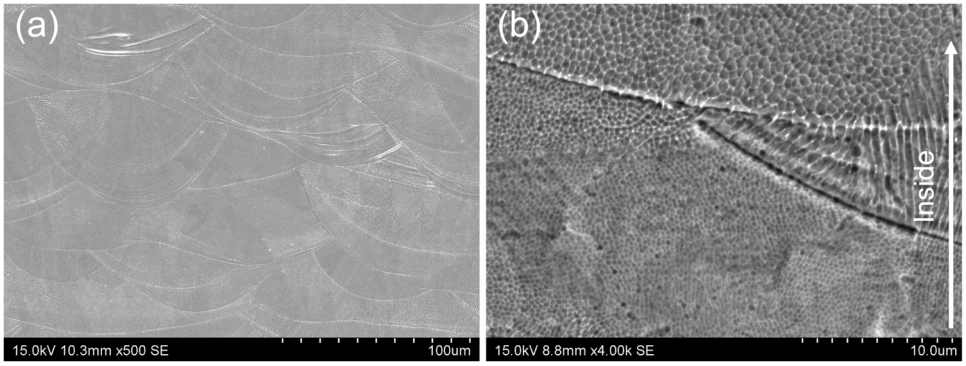

Fig. 4. Microstructure of the 316 L ss parts: General view, (a); detail of the change in the grain size, (b).

as-built samples does not have a negative influence on the variation of the mass. However, it has been seen that the NaCl can be deposited as clusters in the roughness, but these solids can be removed with warm water and do not react with the 316 L ss, so the variation of the mass does not depend on it.

In the acid medium, the samples suffered a loss of mass, regardless of the surface roughness and regardless of exposure time. The sample with the highest roughness (316 L-AB) showed a greater mass loss, probably because of its higher surface area. However, at longer exposure times, the mass loss of both specimens (316 L-AB and 316 L-G) trends to coincide.

3.3. Electrochemical tests

Results of the R_p and the OCP for the samples evaluated in NaCl and H_2SO_4 are shown in Fig. 6. In Fig. 6(a), it can be seen that the surface state had a big influence on the polarization resistance of the samples in the NaCl solution. The as-received specimens showed a lower R_p than the ground ones, having differences of orders of magnitude.

To properly evaluate the value of R_p, it is important to analyze how this value is measured. The equipment polarizes the samples at a value of ΔV and measures the current intensity that appears in the circuit (ΔI). Then the equipment calculates R_p using the area exposed (A) according to Eq. 2.

$$R_p = \frac{\Delta V}{\Delta j} = \frac{\Delta V}{\frac{\Delta I}{A}} \tag{2}$$

However, if the real area is greater than the apparent area, i.e., due to the roughness, the area of the sample is greater than the geometrical area of the hole in the electrochemical cell used, there would be a difference in the actual value of the R_p and the value provided by the equipment solely because of the difference in the area of the sample. The operation is shown in Eq. 3. Where $R_{p_{real}}$ is the value that intrinsically explains the behavior of the material while R_p is the value provided by the equipment if the geometrical surface of the electrochemical cell is used.

$$R_{p_{real}} = \frac{\Delta V}{\frac{\Delta I}{A_{real}}} = \frac{\Delta V}{\frac{\Delta I}{A_{apparent}} \cdot \frac{A_{apparent}}{A_{real}}} = \frac{\Delta V}{\Delta j} \frac{A_{real}}{A_{apparent}} = R_p \frac{A_{real}}{A_{apparent}} \tag{3}$$

By considering this effect, it can be deduced that a correction in the R_p values obtained for the samples should be included, as there is a big difference in the real areas of the samples. From the optical profilometry, by analyzing the profile roughness parameters it has been determined that the real surface for the samples was $\times$ 8.2 $\pm$ 0.1 for the as-built sample and $\times$ 1.01 $\pm$ 0.1 for the ground one. It can be observed that even after applying this correction, there is still a substantial difference in the R_p of the samples, and with different directions in different instants of the test. Therefore, the material at the surface of the two samples had a different behaviour in the corrosion tests apart from the roughness.

On the other hand, the as-received specimens had a decreasing R_p during the first hours until they reached a constant value in less than 48 h. The ground samples had a very different behavior: during the first hours, the samples showed an increase of R_p, and in the following hours this parameter tended to decrease. This different evolution indicates that the corrosion resistance of parts in the as-built state, i.e., with high roughness values, initially reduced with time until they reached a steady-state value, showing that a stable state of the surface was achieved. On the other hand, ground samples, i.e., with low roughness, improved their corrosion resistance in the first hours, but later this parameter decreased.

The evolution of the R_p values with the immersion time in the acidic medium followed the same trend shown in the chloride solution (Fig. 6 (a)). The lowest R_p values were obtained for the 316 L-AB sample. As shown, the polarization resistance of this sample decreased with the increase of the immersion time. At 1 h of immersion time, both samples had almost the same R_p value, but this value increased with the increase of the immersion time for the 316 L-G sample, reaching a value of about 330 kΩ cm^2. Even so, the polarization resistance of the samples was lower in acidic media than in NaCl, being this difference greater between 48 and 216 h of immersion. However, the main conclusion of this analysis is to understand how the sample surface finish affects the R_p values much more than the electrolyte composition.

In general, the corrosion potential (E_{corr}) is indicative of the thermodynamic characteristics of the reaction systems. In the case of the Open Circuit Potential (Fig. 6(b)), similar behavior can be observed, where these values get stabilized over time. In addition, there were big differences in the OCP between the specimens with roughness and without it, for the two media studied, as seen in the case of the polarization resistance and other studies [33]. In general, nobler values were obtained for the samples tested in the acidic media. In contrast with the behavior shown for R_p values, the OCP is more influenced by the media rather than the surface state.

According to several references, the influence of the roughness in the corrosion behavior can be explained by different factors. The first one is that roughness increments the area of the specimen, having more surface exposed to the corrosive phenomena. In the present case, the ratio between A_{real} and $A_{apparent}$ was 8.2. If this factor is considered, in the NaCl

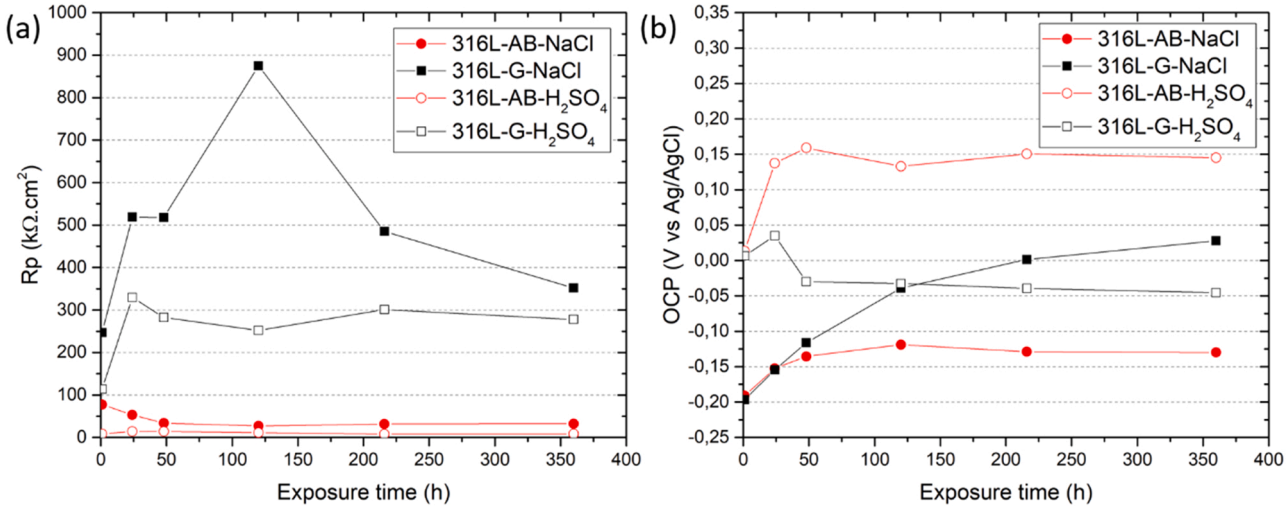

Fig. 6. Electrochemical tests in NaCl and H_2SO_4 solutions: (a) R_p and (b) OCP representation.

solution the Rp in the first hours of immersion is higher in the 316 L-AB than in the 316 L-G, but this changes in the next hours, when the Rp of the 316 L-AB decreases and the area factor is less relevant. However, this fact has no relevance to the R_p of these specimens when they are immersed in the H_2SO_4 solution, indicating that the area factor is less predominant in this particular case. In addition, the presence of this roughness was formed by ellipsoidal big balls, which increments the wettability of the specimen. Some studies claim that the contact angle of the surface in the samples made by SLM is lower than in specimens made by other conventional methods, whose roughness is lower [34], which can involve increasing the corrosion susceptibility in wet environments. A lower contact angle implies the formation of more extended liquid films on the surface while a higher contact angle means that the liquid forms more rounded droplets, which involves a more hydrophobic behavior. Consequently, the roughness of the samples fabricated by SLM causes a better contact between the specimen and the solution, provoking a bigger corrosive attack. Finally, the balling phenomenon has been associated with the formation of linked to surface cracks that also reduce the corrosion resistance of the specimen. [28].

A comparison of the sample surfaces after the electrochemical test is shown in Fig. 7. These micrographs correspond to the samples used in the resistance polarization test of 316 L-AB (Fig. 7(a)) and 316 L-G (Fig. 7(b)) after 360 h of immersion in NaCl 3.5 wt%. It is possible to see the pits formed on the surface of the 316 L-AB sample, but these were not seen on the surface of the 316 L-G sample. The roughness of the 316 L-AB samples increased by 22% after the immersion tests, and some oxidized zones are shown on the surface of the sample immersed in NaCl medium (Fig. 7(c)).

Results of the cyclic polarization tests in NaCl solution are shown in Fig. 8(a) and 8 (b). From the curves, the values of E_{corr} and i_{corr} shown in Table 3 were obtained following the ASTM G3–89 standard, which are of application in the case of systems that have a single time constant near the corrosion potential. Although no differences can be seen over time in the pitting corrosion behavior, there are differences between each type of specimen. In both media, specimens in the as-built state had a more active potential and higher current density than ground samples, which implies that, again, the as-built surface caused a detrimental effect on the corrosion behavior. In addition, a positive hysteresis loop can be seen in the curves obtained with the 316 L-AB samples, which involves the metastable nucleation and growth of pits, something that did not occur in the parts without roughness.

There are several causes besides the ones mentioned before. First, grinding eliminates the impurities and imperfections [35] of the surface that cause differences between zones that can promote the apparition of the pitting corrosion [36]. On the other hand, a reduction of the roughness minimizes the points at which the pits can nucleate, although when the pits do nucleate they grow better in specimens without roughness than on pieces with roughness. Burstein and Pistorius [37] claimed that the origin of this observation was in the geometry of the sites. They found that a more deeply pit site had a greater probability of being activated into diffusion-controlled dissolution, but it grew at a smaller current density.

Fig. 8(c) and (d) show the cyclic polarization curves obtained for 316 L-AB and 316 L-G samples after 1 and 360 h of immersion in the acidic medium, and the values of E_{corr} and i_{corr} are shown in Table 3. Regardless of the immersion time, the 316 L-AB remained passivated, without the breaking down of the passive layer, and in contrast to the NaCl solution, 316 L-G was passivated in the acidic media. Some authors suggest that various stainless steels that have molybdenum as a minor alloying element in their composition, are spontaneously passivated in non-oxidizing acids like H_2SO_4 [38]. Alloys that have noble elements in their composition can form a strong passive layer on their surfaces and, therefore, this passive layer increases the corrosion resistance of the stainless steel [39]. The surface treatment performed on the 316 L-G sample removes the initial passive film and allows a new, more resistive passive film, enriched in molybdenum, to be formed on the surface of 316 L stainless steel when exposed to an acid medium [40], taking the sample to a nobler potential, as previously seen in R_p tests. This can also explain the results obtained in the immersion tests, where a more resistive passive film allowed to reduce the mass loss for the 316 L-G sample (Section 3.2).

Finally, several surface treatments like the grinding can cause in

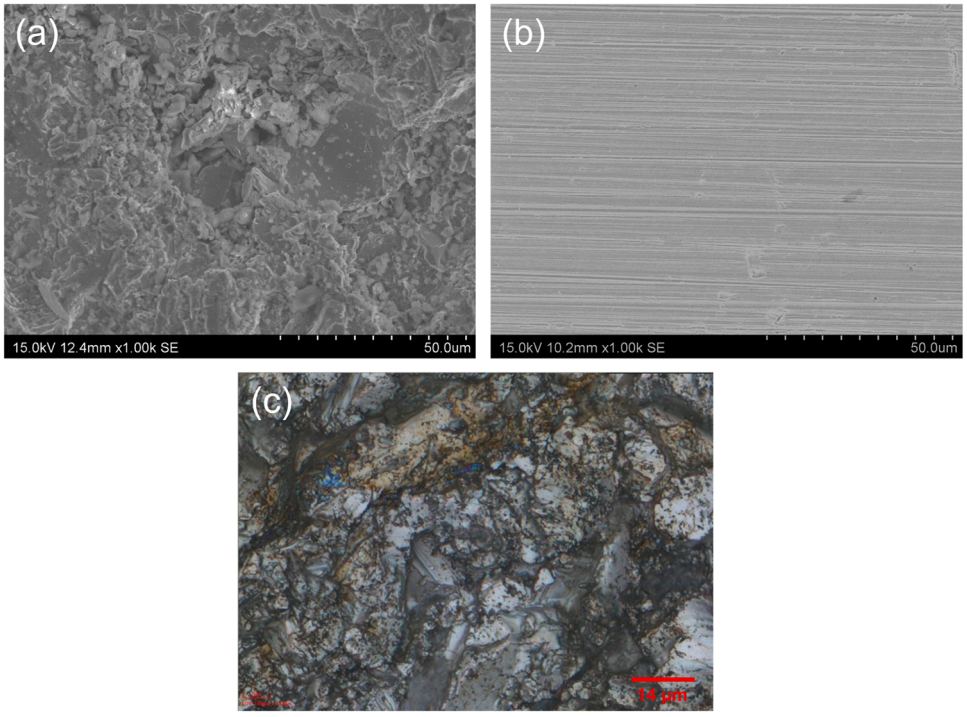

Fig. 7. Surface characterization by SEM of the 316 L stainless steel exposed to 3.5 wt% NaCl for 360 h: (a) 316 L-AB and (b) 316 L-G. (c) Surface profilometer image of 316 L-AB exposed to 3.5 wt% NaCl for 360 h.

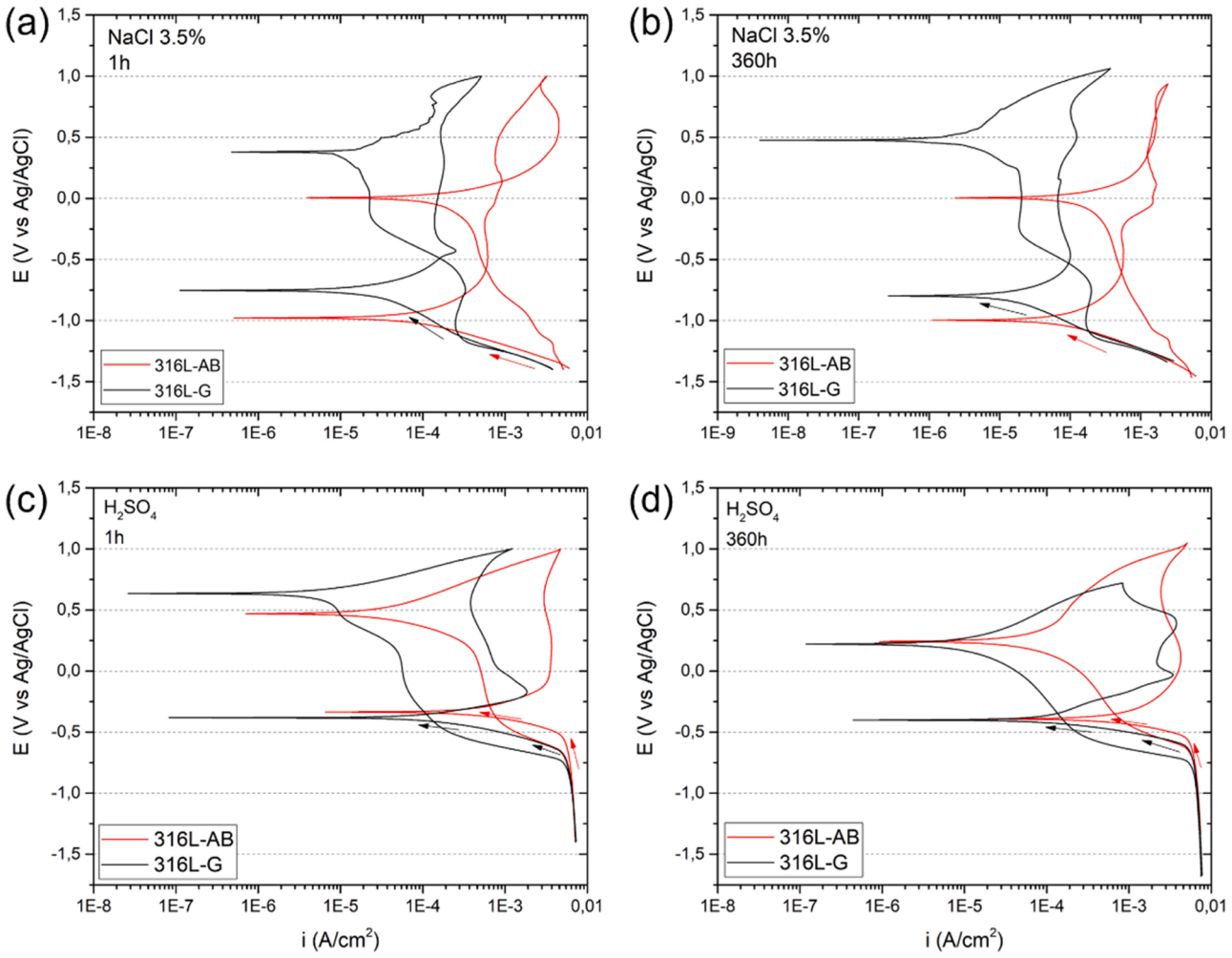

Fig. 8. Cyclic potentiodynamic polarization curves of 316 L-AB and 316 L-G at: (a) 1 h and (b) 360 h of immersion in NaCl 3.5 wt%; and (c) 1 h and (d) 360 h of immersion in H_2SO_4 3 wt%.

Table 3
Corrosion potential (E_{corr}) and corrosion densities (i_{corr}) of the specimens in contact with 3.5 wt% NaCl and 3 wt% H_2SO_4 electrolytes obtained from the cyclic polarization curves after 1 h and 360 h of immersion.

Sample	Electrolyte	Time of immersion (h)	E_{corr} (V)	i_{corr} (μA/cm^2)
316 L-AB	NaCl	1	-0.977	106.2
316 L-G	NaCl	1	-0.748	17.3
316 L-AB	NaCl	360	-0.994	51.8
316 L-G	NaCl	360	-0.794	9.6
316 L-AB	H_2SO_4	1	-0.338	323.1
316 L-G	H_2SO_4	1	-0.375	103.4
316 L-AB	H_2SO_4	360	-0.392	217.1
316 L-G	H_2SO_4	360	-0.395	93.5

steels like the 316 L a nanocrystallization, as was observed by Oleksak et al. [41]. This grain refinement has been found in the steels of this study and can be seen in Table 1 from the broadening of the peaks of the XRD in Fig. 3. In this way, Nowak et al. claimed that the grinding results in higher compressive stress than in the case of the surface of the non-grinded specimens and that this compressive stress causes a more protective oxide on the surface [42]. This difference in the oxide layers between a ground material and a as-built material can be seen in the cyclic polarization for both environments, where the pitting corrosion behavior was better for the ground specimens.

3.4. High-temperature oxidation tests

High-temperature oxidation behavior of the 316 L stainless steel has been evaluated as a function of surface finishing. Mass gain versus time of both as-built and ground 316 L specimens after 360 h of exposure at 800 ºC has been represented in Fig. 9. The results show a huge influence of surface roughness on the high-temperature oxidation resistance of the 316 L: the grinding reduces the mass gain. The as-built sample gained 0.46 ± 0.05 mg/cm^2 after 360 h, while the ground sample only gained 0.22 ± 0.07 mg/cm^2 for the same exposure time. Fig. 9 also shows that mass gain increases markedly during the first 24 h and then tends to slow, particularly in the rough sample. This behavior is characteristic of corrosion kinetics that can be adjusted to a parabolic law (Eq. 4), where the growth of a protective oxide scale on the surface during the first hours reduces the corrosion rate with time. This type of corrosive process is controlled by the diffusion of alloying elements through the layer of oxidized products, mainly Fe, Mn, and Cr, for the case of 316 L stainless steel. Kinetic constants (k_p) of the 316 L-AB and 316 L-G samples are $8.9 \cdot 10^{-4}$ and $1.6 \cdot 10^{-4}$ mg^2/cm^4·h, respectively.

$$(\Delta m/A)^2 = k_p \cdot t \quad (4)$$

These results demonstrate that the original roughness causes more oxidation and accelerates corrosion mainly because as-built materials possess a higher surface-to-volume ratio than ground ones. However, other authors as Nowak et al. [43], who analyzed the effect of surface roughness on high-temperature oxidation of an AISI 316Ti stainless

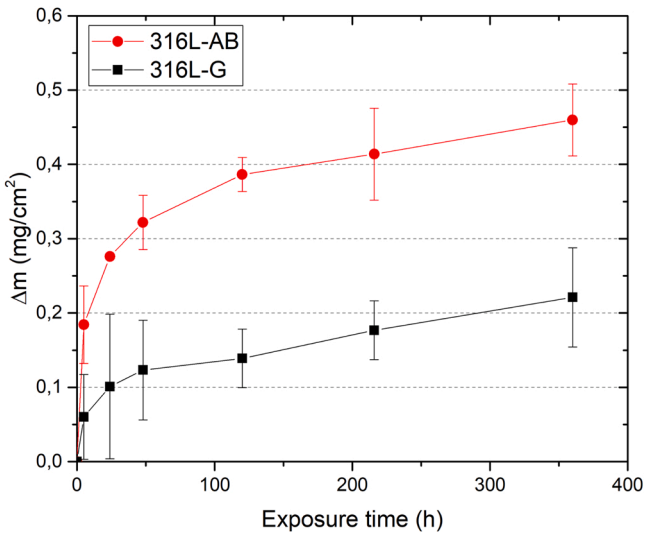

Fig. 9. Mass gain (in mg/cm^2) with time in function of the surface state of 316 L stainless steel.

steel, observed that rougher samples had better oxidation resistance by the combined effect of introduced defects in the near-surface region and the increase of residual stresses caused by mechanical surface preparation. These defects are believed to be an easy diffusion path for elements forming the protective oxide scales, which results in a faster formation of the protective oxide layer. In the same line, Ghosh et al. [44] analyzed the effect of surface working operations on the high-temperature oxidation of AISI 304 L ss and they achieved similar conclusions. The high density of defects presented near the worked surfaces, such as grain boundaries and dislocations, provides an easy diffusion path for oxide scale-forming elements. Similar conclusions were achieved in other works which analyze the effect of surface roughness on different Ni-base alloys [45], [46]. In this context, the results provided in Table 1 for the as-built and the ground samples also show some differences in crystal size and lattice strain between both samples, and these could also justify the differences observed in the mass gain.

The oxide scale formed on 316 L after 360 h at 800 ºC has been analyzed by XRD and the peaks shown in Fig. 10 revealed the formation of the same oxides in both specimens and these were assigned to Fe_2O_3, Cr_2O_3, and $(MnFe)Cr_2O_4$. In both specimens, γ-Fe peaks are still the predominant ones after their exposure to 800 ºC for 360 h and this can be attributed to the thin thickness of the grown oxide scale.

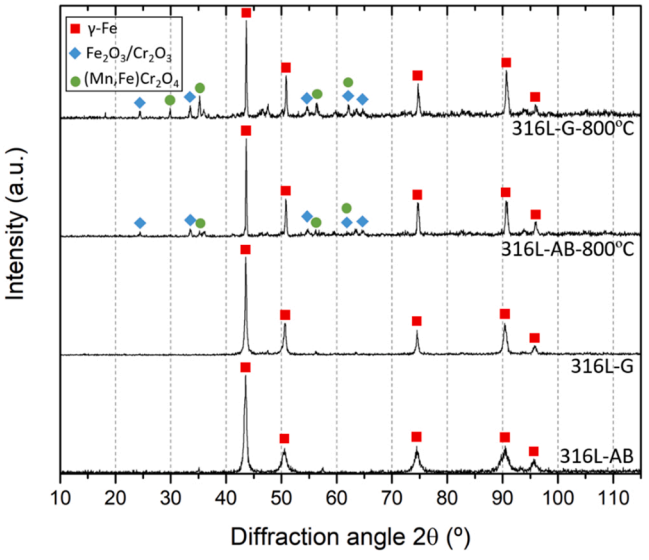

Fig. 10. XDR analysis of the as-built and ground 316 L stainless steel and after corrosion test at 800 °C for 360 h.

Fig. 11 shows cross-sectional SEM micrographs of the 316 L-G and 316 L-AB samples, and, this way, the spinel and corundum oxides identified by XRD have been analyzed. Fig. 11 (a) and Fig. 11 (b) show the cross-sections of the 316 L-AB sample after its exposure to 5 and 360 h at 800 ºC, respectively. The formation of a continuous oxide scale has not been identified and the oxides were heterogeneously distributed along the as-built surface. The presence of grooves avoided the formation of a dense, uniform, and continuous layer of oxides. The punctual EDX performed in the oxide scale of the 316 L-AB sample after its exposure to 360 h at 800 ºC revealed the presence of 45.1Cr, 33.1 O, 6.8Mn, 2.2Ni, 0.9Mo, and Bal. Fe (in wt%). These values are in agreement with the composition of the spinel oxides identified previously by XRD.

The SEM images of the cross-sections of the 316 L-G sample exposed to 5 h (Fig. 11 (c)) and 360 h (Fig. 11 (d)) at 800 ºC revealed that a smooth and uniform oxide scale was grown (arrowed in Fig. 11 (c) and (d)) and the formation of cracks within the oxide scale was avoided. No significant variations were observed between samples exposed to 5 and 360 h for the 316 L-G condition and only an increase of oxide thickness has been distinguished: ~0.5 μm for 5 h against ~2 μm thickness for 360 h. Again, punctual EDX analyses were performed in the oxide scale of the 316 L-G sample after its exposure to 360 h at 800 ºC and its composition (in wt%) was 26.2Cr, 29.2 O, 2.3Mn, 4.2Ni, 1.7Mo, and Bal. Fe.

The plain view of the tested samples has been also analyzed by SEM to complete the characterization of the oxides after their exposure at 800 ºC for 360 h. Two types of oxides were identified in the as-built 316 L-AB sample according to the differences observed in their morphology, as Fig. 11(a) shows. The first ones, marked with red scattered arrows in Fig. 12 (a), have the characteristic morphology of small octahedral crystals of around ~4 μm and they are associated with the formation of Cr-base oxides, as Cr_2O_3 or $MnCr_2O_4$, identified previously in the XRD of Fig. 9. The second ones, identified with yellow arrows in Fig. 12 (a), have laminar morphology and they are associated with the formation of Fe-rich oxides, such as Fe_2O_3 and $FeCr_2O_4$, also identified in the XRD of Fig. 10. These two types of oxide morphologies were identified previously in an AISI 304 stainless steel exposed to 850 ºC in the same dry air atmosphere [47]. Moreover, in the ground 316 L-G samples, one type of oxide was predominant according to its morphology, as Fig. 12 (b) shows. The oxides have the octahedral morphology of Cr-base oxides, such as Cr_2O_3 or $MnCr_2O_4$, and they are homogeneously distributed along the surface.

3.5. Comparison of the influence of the roughness in the three environments

A comparison of roughness influence in the three environments has been done. In this way, a similar trend can be found in the variation of the mass of the specimens immersed in NaCl and H_2SO_4 solutions: grinding the as-built surface up to 2500 cannot reduce the variation of the mass in the NaCl solution but can reduce the loss of mass around 84% in H_2SO_4 solution, showing a great dependence of the parts to this parameter in the second medium. On the other hand, the original surface has also a big influence when the parts are exposed to oxidation at high temperatures. In this case, grinding the surface can reduce the mass gain by 52%. This indicates that the negative influence of the original roughness is higher in H_2SO_4 solutions, where the topography and the composition of the surfaces are more influential than in the case of oxidation at high temperatures, where the corrosion is more homogeneous due to the higher aggressiveness of the environment.

Besides the results obtained in the mass variation measures, the polarization resistance of the studied parts shows huge differences. In the case of the NaCl solution, the ground specimen had a polarization

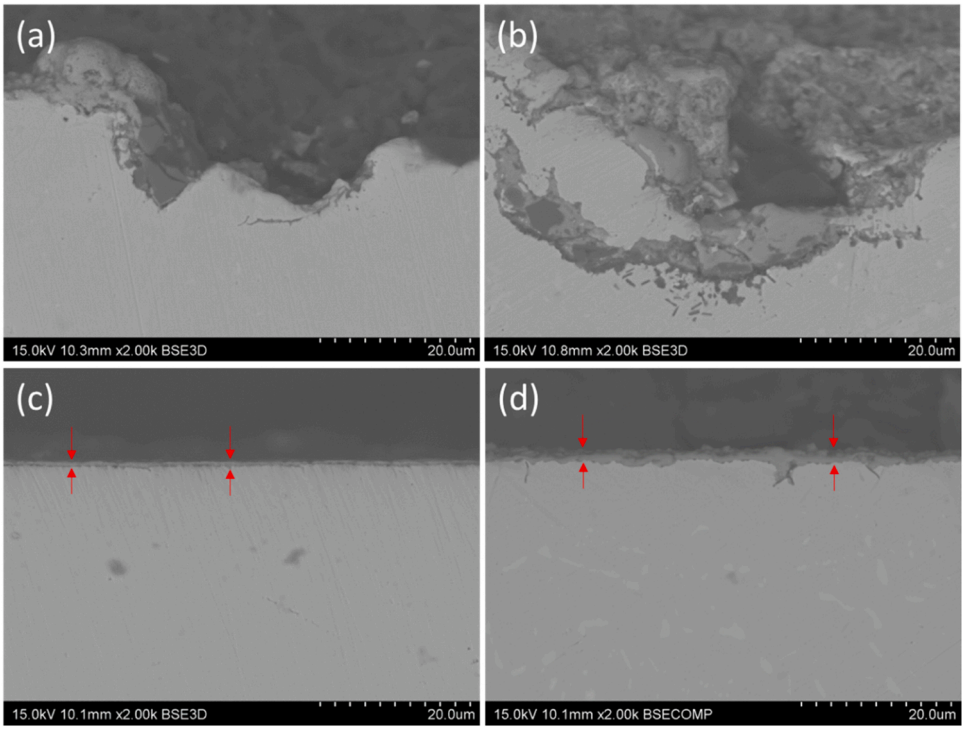

Fig. 11. Cross-sectional SEM characterization of the 316 L-AB sample exposed for (a) 5 h and (b) 360 h, and of the 316 L-G sample exposed for (c) 5 h and (d) 360 h to dry air atmosphere at 800 ºC.

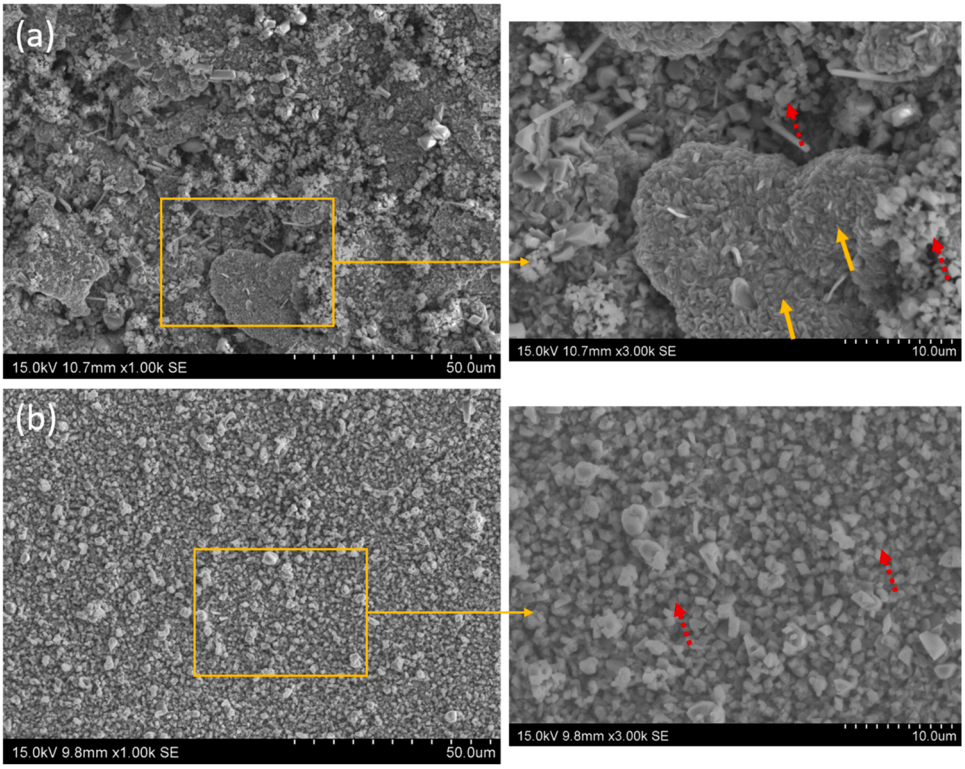

Fig. 12. SEM micrographs from the surface of the 316 L stainless steel exposed to 800 ºC for 360 h: (a) 316 L-AB and (b) 316 L-G.

resistance that was one order of magnitude higher than in the case of the as-built specimen. Also, the ground part showed more than one order of magnitude higher polarization resistance than in the case of the as-built part in the acidic media. This indicates that the polarization resistance is also very dependent on the kind of surface the specimen has and on the type of aggressive solution. In addition, the increment of the surface area due to the roughness can cause a detriment in the corrosion properties, having a worse effect in the NaCl media than in the acidic one. In any case, although the differences between the kinds of aggressive environments are relevant, the influence of the surface state is, again, very

high. This result is particularly important while the complex geometries often obtained by AM processes make it very difficult and sometimes even impossible to apply surface modification techniques, such as grounding, which improves the corrosion resistance of the steel, according to the results described above. In this context, it must be understood that it will not always be possible to carry out surface modification processes to increase the corrosion resistance of parts processed by AM.

4. Conclusions

1. The significant influence of the surface state on the corrosion behavior of the 316 L stainless steel parts manufactured by Selective Laser Melting in different aggressive environments has been established.
2. In the immersion test in NaCl 3.5 wt%, no high differences can be seen between the two kinds of specimens. In the H_2SO_4 medium, the greatest mass loss obtained in the 316 L-AB sample was related to its less protective oxide layer and its higher surface area.
3. Although the polarization resistance values of the 316 L-AB sample stabilize with the immersion time in NaCl, they are, except for the first hours, always lower than those obtained with the ground sample because roughness increment the exposed area of the specimen to the solution, as the predominant factor, and because the original surface has compositional and morphological effects.
4. The detrimental effect of the original surface state was also observed in cyclic polarization curves, where a more active potential and more current density were obtained with as-built surfaces in NaCl. The surface irregularities of the 316 L-AB samples favor the presence of metastable pitting.
5. The better corrosion behavior obtained for the ground sample in H_2SO_4 was related to the formation of a more protective passive layer, formed by better passivation.
6. The high-temperature corrosion tests demonstrated that the grinding process influences the oxidation kinetics of the 316 L stainless steel. The results showed that the grinding process caused less oxidation and decreased the corrosion rates due to a lower surface-to-volume ratio than the original sample.

CRediT authorship contribution statement

J. Bedmar: Methodology, Validation, Formal analysis, Investigation, Data curation, Writing – original draft, Visualization. **N. Abu-warda:** Methodology, Validation, Formal analysis, Investigation, Data curation, Writing – original draft, Visualization. **S. García-Rodríguez:** Methodology, Validation, Formal analysis, Investigation, Data curation, Writing – original draft, Visualization. **B. Torres:** Conceptualization, Formal analysis, Investigation, Resources, Writing – review & editing, Visualization, Supervision, Project administration, Funding acquisition. **J. Rams:** Conceptualization, Formal analysis, Investigation, Resources, Writing – review & editing, Visualization, Supervision, Project administration, Funding acquisition.

Declaration of Competing Interest

The authors declare that they have no known competing financial interests or personal relationships that could have appeared to influence the work reported in this paper.

Data availability

The raw/processed data required to reproduce these findings cannot be shared at this time due to technical or time limitations.

Acknowledgments

The authors wish to thank the Additive Manufacturing: from material to application project, ADITIMAT-CM (reference S2018/ NMT-4411) and Ministerio de Economía, Industria y Competitividad (PID2021–123891OB-I00, PID2021–124341OB-C21) for economical support of the present research.

References

[1] J. Bedmar, A. Riquelme, P. Rodrigo, B. Torres, J. Rams, Comparison of different additive manufacturing methods for 316L stainless steel, Materials vol. 14 (21) (2021) 6504, https://doi.org/10.3390/ma14216504.
[2] N. Rahulan, S.S. Sharma, N. Rakesh, R. Sambhu, A short review on mechanical properties of SLM titanium alloys based on recent research works, Mater. Today Proc. (2021), https://doi.org/10.1016/j.matpr.2021.10.184.
[3] L. Pezzato, M. Dabalà, S. Gross, K. Brunelli, Effect of microstructure and porosity of AlSi10Mg alloy produced by selective laser melting on the corrosion properties of plasma electrolytic oxidation coatings, Surf. Coat. Technol. vol. 404 (2020), 126477, https://doi.org/10.1016/j.surfcoat.2020.126477.
[4] C. Galy, E. Le Guen, E. Lacoste, C. Arvieu, Main defects observed in aluminum alloy parts produced by SLM: From causes to consequences, Addit. Manuf. 22 (2018) 165–175, https://doi.org/10.1016/j.addma.2018.05.005.
[5] M.S. Duval-Chaneac, S. Han, C. Claudin, F. Salvatore, J. Bajolet, J. Rech, Characterization of maraging steel 300 internal surface created by selective laser melting (SLM) after abrasive flow machining (AFM), Procedia CIRP vol. 77 (2018) 359–362, https://doi.org/10.1016/j.procir.2018.09.035.
[6] F. de Oliveira Campos, A.C. Araujo, A.L. Jardini Munhoz, S.G. Kapoor, The influence of additive manufacturing on the micromilling machinability of Ti6Al4V: A comparison of SLM and commercial workpieces, J. Manuf. Process. vol. 60 (September) (2020) 299–307, https://doi.org/10.1016/j.jmapro.2020.10.006.
[7] Y. Tian, et al., Material interactions in laser polishing powder bed additive manufactured Ti6Al4V components, Addit. Manuf. vol. 20 (2018) 11–22, https://doi.org/10.1016/j.addma.2017.12.010.
[8] S. Arunkumar, M.S. Sundaram, K.M. Suketh, S. Vigneshwara, Materials today: proceedings a review on aluminium matrix composite with various reinforcement particles and their behaviour, Mater. Today Proc. no. xxxx (2020), https://doi.org/10.1016/j.matpr.2020.05.053.
[9] Y. Deng, Z. Mao, N. Yang, X. Niu, X. Lu, Collaborative optimization of density and surface roughness of 316L stainless steel in selective laser melting, Materials vol. 13 (7) (. 2020) 1601, https://doi.org/10.3390/ma13071601.
[10] H. Lee, C.H.J. Lim, M.J. Low, N. Tham, V.M. Murukeshan, Y.-J. Kim, Lasers in additive manufacturing: a review, Int. J. Precis. Eng. Manuf. Technol. vol. 4 (3) (2017) 307–322, https://doi.org/10.1007/s40684-017-0037-7.
[11] D. Gu, Y. Shen, Balling phenomena in direct laser sintering of stainless steel powder: metallurgical mechanisms and control methods, Mater. Des. vol. 30 (8) (2009) 2903–2910, https://doi.org/10.1016/j.matdes.2009.01.013.
[12] R. Li, J. Liu, Y. Shi, L. Wang, W. Jiang, Balling behavior of stainless steel and nickel powder during selective laser melting process, Int. J. Adv. Manuf. Technol. vol. 59 (9–12) (2012) 1025–1035, https://doi.org/10.1007/s00170-011-3566-1.
[13] D. Wang, Y. Liu, Y. Yang, D. Xiao, Theoretical and experimental study on surface roughness of 316L stainless steel metal parts obtained through selective laser melting, Rapid Prototyp. J. vol. 22 (4) (2016) 706–716, https://doi.org/10.1108/RPJ-06-2015-0078.
[14] I. La Fé-Perdomo, J. Ramos-Grez, R. Mujica, M. Rivas, Surface roughness R prediction in Selective Laser Melting of 316L stainless steel by means of artificial intelligence inference, J. King Saud. Univ. - Eng. Sci. no. xxxx (2021), https://doi.org/10.1016/j.jksues.2021.03.002.
[15] G. Strano, L. Hao, R.M. Everson, K.E. Evans, Surface roughness analysis, modelling and prediction in selective laser melting, J. Mater. Process. Technol. vol. 213 (4) (2013) 589–597, https://doi.org/10.1016/j.jmatprotec.2012.11.011.
[16] A.R. Pavan, N. Chandrasekar, B. Arivazhagan, S. Kumar, M. Vasudevan, Study of arc characteristics using varying shielding gas and optimization of activated-tig welding technique for thick AISI 316L(N) plates, CIRP J. Manuf. Sci. Technol. vol. 35 (2021) 675–690, https://doi.org/10.1016/j.cirpj.2021.08.013.
[17] A. Ataollahi Oshkour, S. Pramanik, M. Mehrali, Y.H. Yau, F. Tarlochan, N.A. Abu Osman, Mechanical and physical behavior of newly developed functionally graded materials and composites of stainless steel 316L with calcium silicate and hydroxyapatite, J. Mech. Behav. Biomed. Mater. vol. 49 (2015) 321–331, https://doi.org/10.1016/j.jmbbm.2015.05.020.
[18] F. Bartolomeu, et al., 316L stainless steel mechanical and tribological behavior—A comparison between selective laser melting, hot pressing and conventional casting, Addit. Manuf. vol. 16 (2017) 81–89, https://doi.org/10.1016/j.addma.2017.05.007.
[19] L.A. Arteaga-Hernandez, C.A. Cuao-Moreu, C.E. Gonzalez-Rivera, M. Alvarez-Vera, J.A. Ortega-Saenz, M.A.L. Hernandez-Rodriguez, Study of boriding surface treatment in the tribological behavior of an AISI 316L stainless steel, Wear vol. 477 (2021), 203825, https://doi.org/10.1016/j.wear.2021.203825.
[20] R. Jones, O. Kovarik, S. Bagherifard, J. Cizek, J. Lang, Damage tolerance assessment of AM 304L and cold spray fabricated 316L steels and its implications for attritable aircraft, Eng. Fract. Mech. vol. 254 (2021), 107916, https://doi.org/10.1016/j.engfracmech.2021.107916.

[21] S.K. Lee, S.-H. Yun, H.G. Joo, S.J. Noh, Deuterium transport and isotope effects in type 316L stainless steel at high temperatures for nuclear fusion and nuclear hydrogen technology applications, Curr. Appl. Phys. vol. 14 (10) (. 2014) 1385–1388, https://doi.org/10.1016/j.cap.2014.08.006.
[22] E. Liverani, S. Toschi, L. Ceschini, A. Fortunato, Effect of selective laser melting (SLM) process parameters on microstructure and mechanical properties of 316L austenitic stainless steel, J. Mater. Process. Technol. vol. 249 (2017) 255–263, https://doi.org/10.1016/j.jmatprotec.2017.05.042.
[23] Y. Zhao, et al., Improved corrosion performance of selective laser melted stainless steel 316L in deep sea environment, Corros. Commun. (2021), https://doi.org/10.1016/j.corcom.2021.09.002.
[24] S. Periane, et al., Influence of heat treatment on the fatigue resistance of Inconel 718 fabricated by selective laser melting (SLM, Mater. Today Proc. vol. 46 (2021) 7860–7865, https://doi.org/10.1016/j.matpr.2021.02.447.
[25] M. Khomutov, et al., Effect of hot isostatic pressing on structure and properties of intermetallic NiAl–Cr–Mo alloy produced by selective laser melting, Intermetallics vol. 120 (2020), 106766, https://doi.org/10.1016/j.intermet.2020.106766.
[26] G. Ivetic, et al., Fatigue in laser shock peened open-hole thin aluminium specimens, Mater. Sci. Eng. A vol. 534 (2012) 573–579, https://doi.org/10.1016/j.msea.2011.12.010.
[27] P. Tyagi, et al., Reducing the roughness of internal surface of an additive manufacturing produced 316 steel component by chempolishing and electropolishing, Addit. Manuf. vol. 25 (2019) 32–38, https://doi.org/10.1016/j.addma.2018.11.001.
[28] Y. Sun, R. Bailey, A. Moroz, Surface finish and properties enhancement of selective laser melted 316L stainless steel by surface mechanical attrition treatment, Surf. Coat. Technol. vol. 378 (2019), 124993, https://doi.org/10.1016/j.surfcoat.2019.124993.
[29] S. Panda, S.K. Roy Chowdhury, M. Sarangi, Effects of non-Gaussian counter-surface roughness parameters on wear of engineering polymers, Wear vol. 332–333 (2015) 827–835, https://doi.org/10.1016/j.wear.2015.01.020.
[30] B.R. Chrcanovic, A. Wennerberg, M.D. Martins, Influence of temperature and acid etching time on the superficial characteristics of Ti, Mater. Res. vol. 18 (5) (2015) 963–970, https://doi.org/10.1590/1516-1439.014115.
[31] L. Lemarquis, P.F. Giroux, H. Maskrot, B. Barkia, O. Hercher, P. Castany, Cold-rolling effects on the microstructure properties of 316L stainless steel parts produced by Laser Powder Bed Fusion (LPBF), J. Mater. Res. Technol. vol. 15 (2021) 4725–4736, https://doi.org/10.1016/j.jmrt.2021.10.077.
[32] L. Chang, et al., Effect of machining on stress corrosion crack initiation in warm-forged type 304L stainless steel in high temperature water, Acta Mater. vol. 165 (2019) 203–214, https://doi.org/10.1016/j.actamat.2018.11.046.
[33] L. Abosrra, A.F. Ashour, S.C. Mitchell, M. Youseffi, Corrosion of mild steel and 316L austenitic stainless steel with different surface roughness in sodium chloride saline solutions, WIT Trans. Eng. Sci. vol. 65 (2009) 161–172, https://doi.org/10.2495/ECOR090161.
[34] S. Dwivedi, A. Rai Dixit, A. Kumar Das, Wetting behavior of selective laser melted (SLM) bio-medical grade stainless steel 316L, Mater. Today Proc. (2021), https://doi.org/10.1016/j.matpr.2021.12.046.
[35] P. Gümpel, A. Hörtnagl, Influence of the surface condition on corrosion behavior of stainless steel, Mater. Corros. vol. 67 (6) (2016) 607–620, https://doi.org/10.1002/maco.201608893.
[36] P. Fajnor, T. Liptáková, V. Konstantová, INFLUENCE OF AISI 316Ti STAINLESS STELL SURFACE TREATMENT ON PITTING CORROSION IN VARIOUS SOLUTIONS, Mater. Eng. vol. 17 (3) (2010) 21–27. ⟨http://fstroj.uniza.sk/journal-mi/PDF/2010/04-03.pdf⟩.
[37] G.T. Burstein, P.C. Pistorius, Surface roughness and the metastable pitting of stainless steel in chloride solutions, CORROSION vol. 51 (5) (1995) 380–385, https://doi.org/10.5006/1.3293603.
[38] S. Kannan, A. Balamurugan, S. Rajeswari, H2SO4 as a passivating medium on the localised corrosion resistance of surgical 316L SS metallic implant and its effect on hydroxyapatite coatings, Electrochim. Acta vol. 49 (15) (2004) 2395–2403, https://doi.org/10.1016/j.electacta.2004.01.003.
[39] P. Peled, D. Itzhak, The surface composition of sintered stainless steel containing noble alloying elements exposed to a H2SO4 environment, Corros. Sci. vol. 32 (1) (1991) 83–90, https://doi.org/10.1016/0010-938X(91)90064-V.
[40] I. Olefjord, B.-O. Elfstrom, The composition of the surface during passivation of stainless steels, Corrosion vol. 38 (1) (1982) 46–52, https://doi.org/10.5006/1.3577318.
[41] R.P. Oleksak, G.R. Holcomb, C.S. Carney, L. Teeter, Ö.N. Doğan, Effect of surface finish on high-temperature oxidation of steels in CO_2, supercritical CO_2, and air, Oxid. Met. vol. 92 (5–6) (2019) 525–540, https://doi.org/10.1007/s11085-019-09938-6.
[42] W.J. Nowak, K. Siemek, K. Ochał, B. Kościelniak, B. Wierzba, Consequences of different mechanical surface preparation of Ni-base alloys during high temperature oxidation, Materials vol. 13 (16) (2020) 3529, https://doi.org/10.3390/ma13163529.
[43] W.J. Nowak, Effect of surface roughness on oxidation resistance of stainless steel AISI 316Ti during exposure at high temperature, J. Mater. Eng. Perform. vol. 29 (12) (2020) 8060–8069, https://doi.org/10.1007/s11665-020-05267-x.
[44] S. Ghosh, M.K. Kumar, V. Kain, High temperature oxidation behavior of AISI 304L stainless steel—Effect of surface working operations, Appl. Surf. Sci. vol. 264 (2013) 312–319, https://doi.org/10.1016/j.apsusc.2012.10.018.
[45] D. Serafin, W.J. Nowak, B. Wierzba, Differences in oxides morphology as a result of surface preparation of NiFe alloy, Surf. Coat. Technol. vol. 385 (2020), 125421, https://doi.org/10.1016/j.surfcoat.2020.125421.
[46] W. Nowak, Effect of surface roughness on early stage oxidation behavior of Ni-base superalloy IN 625, Appl. Syst. Innov. vol. 1 (3) (2018) 32, https://doi.org/10.3390/asi1030032.
[47] N. Abu-warda, A.J. López, M.D. López, M.V. Utrilla, High temperature corrosion and wear behavior of HVOF-sprayed coating of Al2O3-NiAl on AISI 304 stainless steel, Surf. Coat. Technol. vol. 359 (2019) 35–46, https://doi.org/10.1016/j.surfcoat.2018.12.047.